Resonant soft X-ray diffraction – *in extremis*

P. D. Hatton,[a]* S. B. Wilkins,[b,c] T. A. W. Beale,[a] T. K. Johal,[d] D. Prabhakaran[e] and A. T. Boothroyd[e]

[a]Department of Physics, University of Durham, Rochester Building, South Road, Durham DH1 3LE, UK, [b]European Commission, Joint Research Center, Institute for Transuranium Elements, Hermann con Helmholtz-Platz 1, 76344 Eggenstein-Leopoldshafen, Germany, [c]ESRF, BP 220, F-38043 Grenoble CEDEX, France, [d]CCLRC Daresbury Laboratory, Warrington WA4 4AD, UK, and [e]Department of Physics, University of Oxford, Clarendon Laboratory, Parks Road, Oxford OX1 3PU, UK. E-mail: p.d.hatton@dur.ac.uk

The use of softer-energy X-rays produced by synchrotron radiation for diffraction is an area of current interest. In this paper, experiments exploiting resonant scattering at the L absorption edges of $3d$ transition metal elements are reported. Such energies, typically 500–1000 eV, are at the extreme limit of soft X-ray diffraction where absorption effects are so severe that the sample and diffractometer must be placed in a windowless high-vacuum vessel. In addition, the Ewald sphere is so small as to likely contain, at most, only a single Bragg reflection. Advantages of using such radiation for the study of weak diffraction effects such as anomalous scattering, charge ordering, magnetic diffraction and orbital ordering are reported.

Keywords: soft X-rays; magnetic diffraction; orbital ordering; resonance effects.

1. Introduction

X-ray diffraction has typically employed laboratory X-ray sources which use electron bombardment of metal targets to produce X-rays in the energy range 8–15 keV. Using laboratory sources normally restricts the choice of X-ray energies to particular emission lines such as Cu $K\alpha$. Use of a synchrotron allows access to a wide range of X-ray energies that can be continuously tuned, typically by varying the monochromator angle (Als-Nielsen & McMorrow, 2001). However, in spite of this wide range of possible energies, most diffraction experiments have continued to employ X-ray energies of 8–15 keV. The choice is mainly determined by sample absorption and fluorescence. In the last few years the use of anomalous scattering (*e.g.* at the selenium edge) has been used for phasing crystallographic diffraction from single crystals, particularly of biomaterials (Fourme *et al.*, 1995). In tandem, other studies have employed resonant scattering at absorption edges to study magnetic and multipolar ordering. With photon energies close to favourable absorption edges, X-ray magnetic intensities can be resonantly enhanced from barely detectable levels (Hannon *et al.*, 1988; Blume, 1985). This has provided a high wavevector resolution element-specific technique complementary to neutron magnetic scattering utilizing the M edges of actinide elements (Isaacs *et al.*, 1989) and the more modest L-edge resonances of the lanthanides (Gibbs *et al.*, 1988). This has led to an ever-widening range of X-ray energies required at synchrotron radiation sources employing insertion devices such as wigglers and undulators. Higher X-ray energies are useful for extending the size of the Ewald sphere, and hence the quantity of the accessible diffraction pattern as well as minimizing sample absorption, and as a probe of bulk samples such as stress/strain effects (Hatton *et al.*, 2003). In biological crystals the need to minimize sample damage caused by the incident X-rays and the use of anomalous scattering from crystals not containing heavy elements has extended interest in the use of softer X-rays down to 6 keV (Weiss *et al.*, 2001). Studies of uranium compounds have employed resonant scattering at the uranium M edge, giving huge resonant enhancement of charge and magnetic scattering at energies down to 3.8 keV (Isaacs *et al.*, 1989). At such energies, absorption owing to beryllium windows, air paths, sample *etc.* have to be minimized. Unfortunately the largest class of magnetic materials of technological use and of fundamental research interest containing $3d$ transition metals contain no strong resonances in the hard X-ray region. Studies have shown that the largest resonant enhancements that can be used for X-ray magnetic scattering are those of the $L_{2,3}$ edges in the $3d$ transition metals (Wilkins, Hatton *et al.*, 2003; Thomas *et al.*, 2004; Dhesi *et al.*, 2004; Abbamonte *et al.*, 2002), the $M_{4,5}$ edges for the lanthanides (Gibbs *et al.*, 1988) and the $N_{4,5}$ edges in the actinides (Isaacs *et al.*, 1989). Such absorption edges occur in the soft X-ray region with energies of only 500–1500 eV. Resonant soft X-ray scattering can therefore be used to probe the magnetic structure and interfaces of ultrathin films (Weschke *et al.*, 2004).

2. Experimental technique

Most of our results obtained to date have used station 5U1 at Daresbury, which is equipped with a vacuum-compatible two-circle diffractometer that was designed for multilayer and diffraction-grating efficiency measurements (Roper *et al.*, 2001). The beamline is situated at the end of a variable-gap undulator and produces a tunable beam of photons in the energy range 60–1000 eV. A post-grating exit slit was used, resulting in an energy resolution of $\Delta E = 1$ eV at 640 eV. The incident X-rays are approximately 90% linearly polarized with an incident flux of the order of 10^{11} photons s^{-1}. The diffractometer, shown schematically in Fig. 1, has been subsequently adapted for low-temperature resonant energy soft X-ray measurements. It is a cylindrical vessel of internal diameter 60.5 cm with a horizontal cylinder axis with a concentrically mounted two-circle stage for independent sample (θ) and detector (2θ) rotations. The stepper-motor-driven rotations are external to the cylinder and couple *via* a differentially pumped rotary seal. Almost all of the experiments we have undertaken require low temperatures and therefore the sample goniometer had to be modified to enable measurements at cryogenic temperatures. Fig. 2 shows the inside of the vacuum vessel with the liquid-nitrogen-cooled goniometer that can reach a base temperature of 83 K. The diffractometer operates with a base pressure of 10^{-6} to 10^{-7} torr. A 300 µm slit was placed in front of the detector to increase the experimental resolution, resulting in an angular resolution of $0.1°$. The diffracted beam is detected by an Au/GaAsP Schottky diode whose output is fed into a current-to-voltage amplifier. Typical currents of diffracted beams are approximately 100 nA.

3. Experimental results

For the first attempt at observing soft X-ray diffraction from a single crystal we chose to study the bilayer manganite $LaSr_2Mn_2O_7$ (Moritomo *et al.*, 1996; Wilkins, Spencer, Beale *et al.*, 2003). This material crystallizes in a layered structure as shown in Fig. 3 and has unit-cell parameters of 3.87 Å $\times$

3.87 Å $\times$ 20.1 Å. The *c*-axis is sufficiently long to allow us to access the (002) Bragg reflection at soft X-ray energies. Indeed, under ambient conditions it is the only Bragg reflection within the Ewald sphere at energies corresponding to the
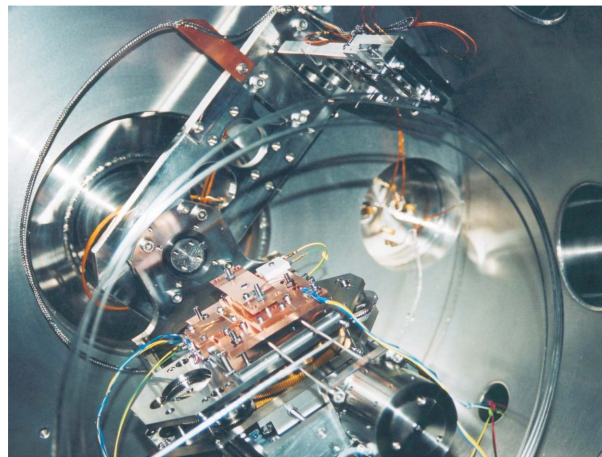

Figure 2
Photograph of the inside of the diffractometer showing the liquid-nitrogen-cooled goniometer. Liquid nitrogen is fed through the small tubes shown in the foreground. The 2θ detector stage can be seen towards the top of the photograph. In this orientation the incident X-ray beam would be from the left.

La, Sr   Mn   O   Mn Spin   Mn Octahedra

$\langle 001 \rangle$ $\langle 010 \rangle$ $\langle 100 \rangle$

Figure 3
Crystallographic and magnetic structure of $LaSr_2Mn_2O_7$, showing the extended *c*-axis producing a highly two-dimensional system.
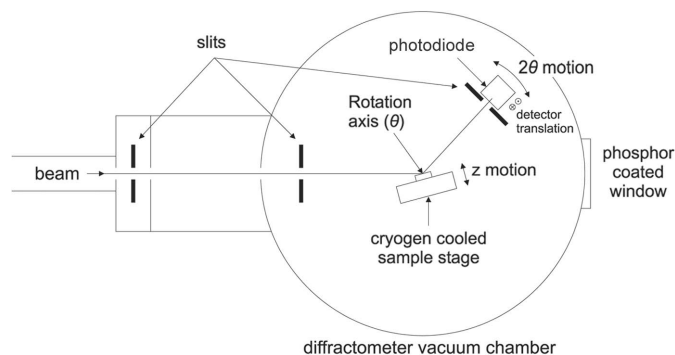

Figure 1
Schematic diagram of the diffractometer shown from the side. The X-ray beam enters from the left-hand side and is scattered from the sample in the centre of the chamber. There is a small translation of the detector (out of the page) which allows a pseudo-χ movement. The sample stage is cooled by liquid nitrogen.
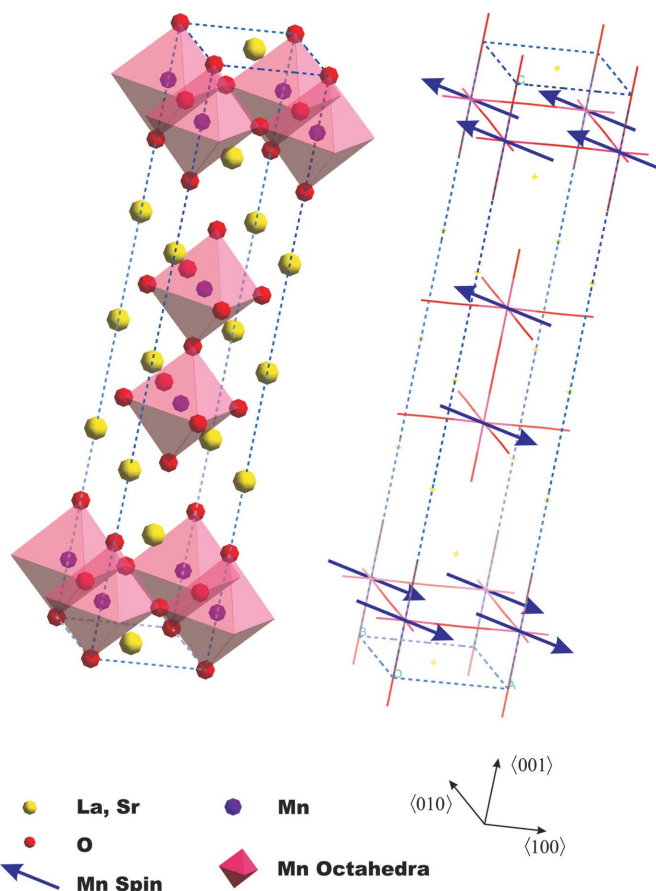
Mn L_2 and L_3 edges. The crystal was grown at the University of Oxford by the floating zone method and had dimensions of 8 mm × 8 mm × 1 mm. Such samples naturally cleave giving large faces with [001] surface normal. We have subsequently found that in order to observe soft X-ray diffraction the surface quality is vital. Samples have to be ground and polished to remove surface damage and contamination because the soft X-rays penetrate only a relatively small distance into the crystal. However, samples which naturally cleave, like the [001] surfaces of the bilayer manganites, require no further preparation and the untreated surface can be used. The sample had been pre-aligned and was mounted on the goniometer with the [001] and [110] directions defining the diffraction plane and the [110] direction being perpendicular to the X-ray electric field vector.

Initial experiments were conducted in the non-resonant condition at 900 eV, well away from any absorption edges. At 900 eV the Bragg angle of 44° ensures that the reflection is easily accessible. Fig. 4 shows a scan through the (002) Bragg reflection in the [00l] direction. The reflection was found to be approximately Lorentzian in shape. Such a scan parallel to the scattering vector measures the crystal truncation rod, and hence the full width at half-maximum gives a measure of the broadening of the peak in reciprocal space caused by the finite penetration of the X-ray beam into the bulk single-crystal. We found the inverse correlation length [defined as $\xi = (2\pi/c)\kappa$, where κ is the half width at half-maximum in units of reciprocal lattice units (r.l.u.) and c is the direct space lattice parameter] to be 2.707×10^{-3} Å^{-1}. This is approximately half the value of the inverse correlation length measured by us on the same crystal at a photon energy of 12.4 keV and is comparable with the absorption attenuation length, μ^{-1}. Thus we conclude that the soft X-ray beam is penetrating through many hundreds of unit cells of the single crystal and effectively probing the bulk of the sample. In spite of previous misconceptions, soft X-ray diffraction is not a particularly surface-sensitive technique requiring specialized sample preparation.
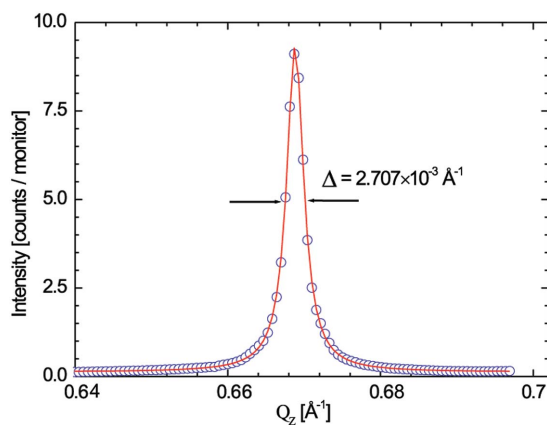
We then recorded the intensity of the Bragg (002) reflections as a function of the incident energy around the L edges of manganese. Close to absorption edges the real and imaginary scattering factors are radically altered giving increased absorption but also increased scattering. Fig. 5 shows the intensity of the (002) reflection in the vicinity of the L_3 and L_2 manganese absorption edges. Changing the energy obviously changes the angular position of the Bragg reflection. However, by scanning at constant wavevector it is possible to continuously stay aligned on the reflection whilst changing the incident X-ray energy. Dramatic enhancements of the diffraction intensity are observed at ~640 and ~655 eV, while the background remained constant. Such large resonant enhancements could not be obtained at other edges and demonstrates the huge resonant enhancements that are possible by working with soft X-rays. Indeed, these enhancements are so large that potentially very weak charge scattering could be easily observed by employing resonant-enhanced scattering. For example, the observation of very weak Bragg scattering could be used to test unit-cell symmetries by testing for systematic absences, or for the study of crystallographic phase transitions. Of course, with only one Bragg peak observable within the Ewald sphere this is not a technique useful for crystallographic structure solution. Samples with very large unit cells (e.g. biomaterials) would have many more allowed reflections.

These charge-scattering measurements already extend the range of possibilities of X-ray diffraction in the study of crystal structures, but the really exciting prospect is the use of such resonances in the study of magnetic structures. The use of X-ray scattering to probe magnetic structures started over 20 years ago (Bergevin & Brunel, 1981) but has developed enormously in the last 15 years at synchrotron radiation sources (Blume & Gibbs, 1988, 1989; Gibbs et al., 1988). Normally, magnetic scattering is ~10^8 times weaker than charge scattering, but this can be resonantly enhanced close to absorption edges. $LaSr_2Mn_2O_7$ undergoes a transition into a charge and orbitally ordered state at 220 K followed by a
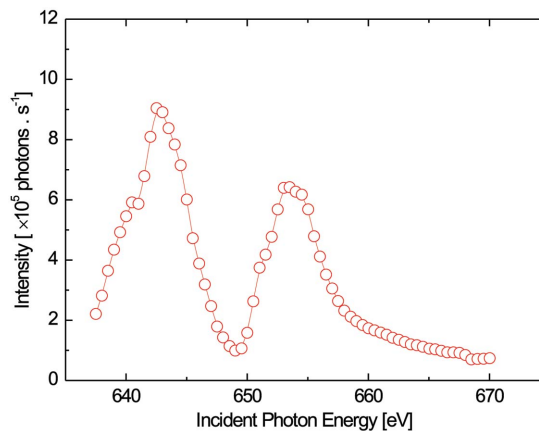

Figure 4
Q_z scan of the (002) Bragg peak in $LaSr_2Mn_2O_7$ at 900 eV. The width is comparable with the attenuation length of the X-rays showing that, although the technique is not particularly surface sensitive, it is resolution limited. The peak is fitted to a Lorentzian lineshape.

Figure 5
Energy scan of the (002) Bragg peak in $LaSr_2Mn_2O_7$ in the vicinity of the Mn L_{II} and L_{III} edges. This shows the resonant enhancement achieved through anomalous scattering.

transition into an A-type antiferromagnetic structure at 180 K (Ling *et al.*, 2000). The magnetic structure has been previously determined by neutron scattering experiments. Fig. 3 shows the low-temperature magnetic structure, which consists of ferromagnetic planes along *ab* stacked antiferromagnetically along the *c*-axis. This causes a magnetic diffraction peak below 180 K to be formed at the (001) position. Above this temperature there is no charge scattering at the (001) position owing to the crystallographic body centring of the tetragonal unit cell.

The sample was therefore cooled to 83 K with the incident photon energy set to the manganese L_3 absorption edge. Soft X-rays with this energy are absorbed by the sample causing a dipolar transition from the $2p_{3/2}$ to the $3d$ levels, hence directly probing the split $3d$ electronic structure owing to the magnetism. This is therefore both an element-specific and band-specific measurement of the magnetism. A scan through the (001) position (shown in Fig. 6) showed considerable intensity, which had not been observed at temperatures above the Néel temperature T_N. Indeed, at 85 K the (001) magnetic reflection had an intensity greater than that of the structural (002) reflection. An energy scan at constant wavevector through the (001) reflection is shown in Fig. 7. This is very different to that of the (002) Bragg structural feature and shows splittings associated with the electronic structure of the $3d$ band. The resonant enhancement at the L_3 edge is particularly large. Magnetic diffraction was also observed at the Mn L_2 edge. However, well away from these energies the magnetic peak was unobservable owing to its very low intensity. Such a large resonant increase in intensity is in line with predictions.

In spite of the advantages of using soft X-ray diffraction with the $3d$ transition metals, there are a number of experimental shortcomings. Although azimuthal analysis has been performed and is discussed in other studies, it is currently only possible on a minority of end stations, and even then it is technically very difficult. In addition, linear polarization is an extremely important technique (Hill & McMorrow, 1996) with resonant studies and has been used effectively at the transi-

tion-metal *K* edges (Murakami, Hill *et al.*, 1998) and the *M* edges of the actinides (Paixao *et al.*, 2002). To date, polarization analysis has not been technically feasible at the transition-metal *L* edges.

4. Discussion

Our results demonstrate the unique features of resonant magnetic diffraction as a probe of the magnetic state of a material. By tuning to different edges it is possible to provide elemental-specific measurements; for example, separating the spin and orbital components of each chemical species in a ferromagnet. Also, the absorption-edge position, and hence the energy of the core–electron transitions, is dependent on the valence. Resonant soft X-ray diffraction can provide this degree of both element and valence-state specificity. Furthermore, these results demonstrate that with soft X-rays we can enter a new regime where magnetic scattering is substantially more intense than charge scattering.

There is another ordering process that occurs in many transition metal compounds, namely orbital ordering (Tokura & Nagaosa, 2000). Orbital ordering, which involves correlations between the spatial distribution of the outermost valence electrons, has long been considered as a vital ingredient in the structural and physical properties of strongly correlated electron systems such as transition metal oxides (Goodenough, 1955). The competition and cooperation between the charge, orbital and spin degrees of freedom of the electron manifests itself in unusual properties such as high-temperature superconductivity, colossal magnetoresistance and magneto-structural transitions.

X-ray diffraction is generally sensitive to the isotropic electron density distribution. However, by tuning the photon energy to an absorption edge, enhanced sensitivity to the valence states is obtained (Hill & McMorrow, 1996). Resonant X-ray scattering (RXS) involves virtual excitations from core to unoccupied states; photons are virtually absorbed by exciting core electrons to empty states, and subsequently re-
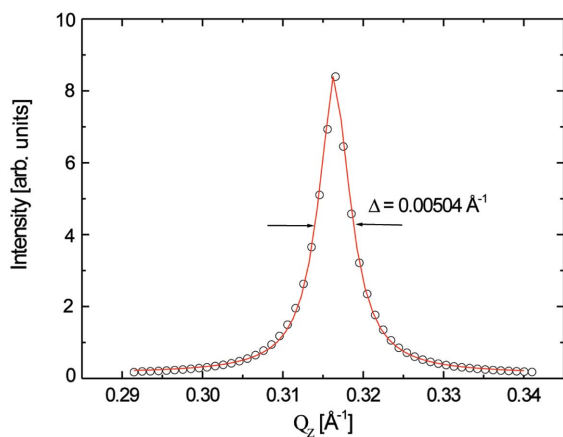

Figure 6
Q_z scan of the (001) magnetic peak in LaSr$_2$Mn$_2$O$_7$ at 83 K. As expected, no signal was present above T_N. The peak is fitted to a Lorentzian squared line-shape.

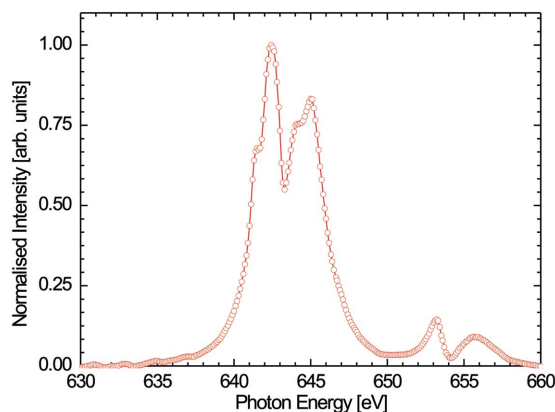**Figure 7**
Energy scan of the (001) magnetic peak in LaSr$_2$Mn$_2$O$_7$ at 83 K showing the huge resonance available at transition metal *L* edges. The resonant enhancement is much large than at the *K* edge, and no peak is detectable off resonance.

emitted when the excited electrons and their core hole recombine. The spin-dependent terms of the scattering cross section are normally assumed to be minimal; however, the resonant scattering case is found when

$$\hbar\omega \simeq E_n - E_0, \qquad (1)$$

where ω is the incident X-ray frequency and E_0 and E_n are the initial and final electron energy levels. As such, the magnetic scattering contribution becomes a significant contributor to the overall scattering, and the spin-dependent term of the total cross section becomes

$$\left(\frac{\hbar^2 k^2}{m}\right)$$

$$\times \sum_{ij}\sum_c \frac{\langle b|(\hat{k}'\times\varepsilon')\cdot\mathbf{s}_j \exp(-i\,\mathbf{k}'\cdot\mathbf{r}_i)|c\rangle\langle c|(\hat{k}\times\varepsilon)\cdot\mathbf{s}_j \exp(i\,\mathbf{k}\cdot\mathbf{r}_j)|a\rangle}{E_a - E_c + \hbar\omega - i\,(\Gamma c)/2},$$

$$(2)$$

where k and k' are the incident and exit photon vectors, ε and ε' are the incoming and diffracted polarization vectors, $|a\rangle$, $\langle b|$ and $|c\rangle$ are the initial, final and intermediate quantum states, $\mathbf{s}_j$ is the atomic scattering factor of the spin of atom j, which is at a distance $\mathbf{r}_j$ from the origin. The term $i(\Gamma c)/2$ is introduced to take account of the energy level width. In the case when (1) is true, (2) is of the order of

$$i\frac{\hbar\omega}{mc^2}\,2\,\frac{\hbar\omega}{\Gamma_c}\sum_{ij}\langle b|\exp(-i\,\mathbf{k}'\cdot\mathbf{r}_i)|c\rangle\langle c|\exp(i\,\mathbf{k}'\cdot\mathbf{r}_j)|a\rangle. \qquad (3)$$

Such scattering can be caused by long-range ordering of magnetic moments, electronic orbital occupancy or aspherical valence electron clouds; and such scattering is element specific. The intensity of the superlattice reflections increases dramatically as the photon energy is tuned to an atomic absorption edge. RXS studies of $LaSr_2Mn_2O_7$ were first attempted at the manganese K edge (Wakabayashi et al., 2000). Resonant diffraction of an orbital ordering reflection displayed a striking increase near the absorption edge and an azimuthal dependence. Unfortunately the orbital order wavevector of $(\frac{1}{4},\frac{1}{4},0)$ means that the reflection cannot be accessed with a sample cut such that [0,0,1] is surface normal. Therefore the only method of observing this reflection is to cut across the cleavage planes at an angle, and the bilayer manganites are very poorly ordered between the $hk0$ planes. However, some indication of the type of data possible can be obtained from the single-layer manganite $La_{0.5}Sr_{1.5}MnO_4$.

In $La_{0.5}Sr_{1.5}MnO_4$ the Mn sites at room temperature are all crystallographically equivalent with an average valency of +3.5. This material displays a phase transition at $\sim$240 K, below which additional reflections at a wavevector of $(\frac{1}{2},\frac{1}{2},0)$ have been observed caused by charge disproportionation of the Mn ions into two inequivalent sites identified as Mn^{3+} and Mn^{4+} (Murakami, Kawada et al., 1998; Sternlieb et al., 1996). Subsequent studies (Daoud-Aladine et al., 2002) have disputed such a simple charge transfer model and rather suggested non-integer charge disproportion into $Mn^{3.5-\delta}$/$Mn^{3.5+\delta}$. Further studies by a number of groups are investi-

gating such charge order. The strong Hund's rule coupling and the large cubic (O_h) component of the crystal field implies that the Mn^{3+} $3d^4$ site has three electrons in the $t_{2g\uparrow}$ level and one electron in the twofold degenerate $e_{g\uparrow}$ level. The degeneracy of the $e_{g\uparrow}$ level can be lifted by cooperative Jahn–Teller distortions of the MnO_6 octahedral reducing the symmetry to D_{4h} and separating the two degenerate levels into $3d_{3z^2-r^2\uparrow}$ and $3d_{x^2-y^2\uparrow}$ levels. The presence of Jahn–Teller distortions leads to additional satellites observed at a wavevector of $(\frac{1}{4},\frac{1}{4},0)$. Therefore, cooperative Jahn–Teller distortions of the MnO_6 octahedra could provide the origin of orbital ordering in the manganites owing to occupation of the $3d_{3z^2-r^2\uparrow}$ or $3d_{x^2-y^2\uparrow}$ orbitals along the elongation direction. An alternative description as to how the orbital ordering may occur was provided by Goodenough (1955). Further cooling below $T_N \simeq$ 110 K results in long-range spin ordering with a wavevector of $(\frac{1}{4},\frac{1}{4},\frac{1}{2})$ and the formation of a complex antiferromagnetic ordering of both manganese sublattices (Sternlieb et al., 1996). The arrangements of the spins in $La_{0.5}Sr_{1.5}MnO_4$ is similar to that adopted by the half-doped manganites, the so-called magnetic CE phase. This structure was intuitively predicted by Goodenough (1955) who also predicted that the spin arrangements would occur via orbital ordering in the higher-temperature phase. Thus the alternative model of orbital
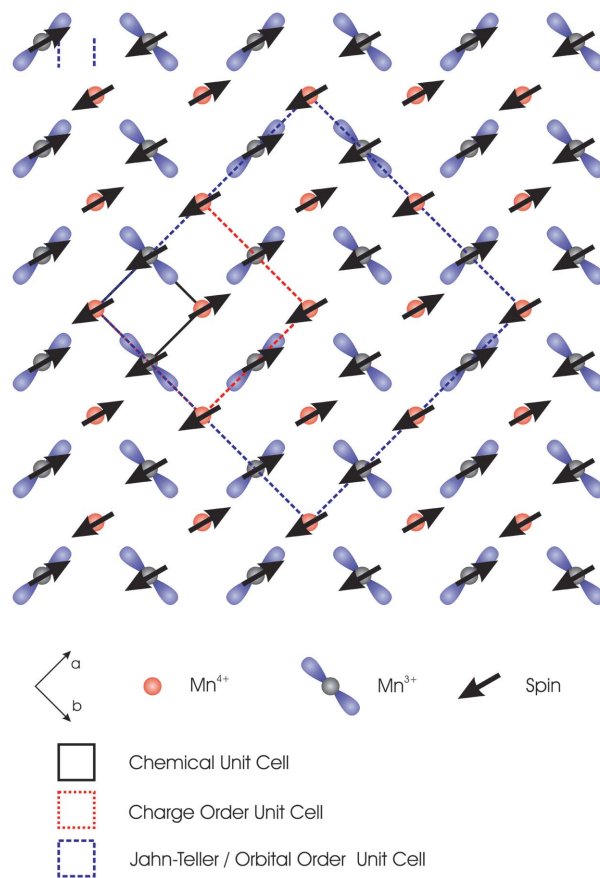

a
b
● Mn^{4+} Mn^{3+} ↖ Spin

☐ Chemical Unit Cell

⬚ Charge Order Unit Cell

⬚ Jahn-Teller / Orbital Order Unit Cell

Figure 8
Charge, orbital and magnetic structure of $La_{0.5}Sr_{1.5}MnO_4$ showing a single ab plane. The orbital order unit cell is four times as large as the $I4/mmm$ chemical unit cell, producing superlattice peaks at $(\frac{1}{4},\frac{1}{4},0)$.

ordering highlights orbital order correlations caused by anti-ferromagnetic spin ordering. Until very recently such questions remained unanswered as direct observation of orbital ordering remained elusive.

The Mn K-edge resonance involves virtual excitations from the $1s$ to the $4p$ band and is thus generally insensitive to orbital ordering of the $3d$ levels. Theoretical studies have proposed that the observed sensitivity is actually caused by Jahn–Teller distortions, $4p$ band structure effects and $3d$–$4p$ Coulomb interactions (Benedetti *et al.*, 2001; Solovyev & Terakura, 1999; Benfatto *et al.*, 1999; Elfimov *et al.*, 1999; Mizokawa & Fujimori, 1997). In order to directly observe $3d$ orbital ordering we need to access the Mn L edges. The first direct observations of orbital ordering using soft X-rays in $La_{0.5}Sr_{1.5}MnO_4$ was reported by Wilkins, Spencer, Hatton *et al.* (2003). Aided by published theoretical predictions (Castleton & Altarelli, 2000), they reported that the shapes of the energy resonances at the Mn L_{III} and L_{II} edges showed that the spectra were caused by a mixture of both cooperative Jahn–Teller distortions and direct Goodenough orbital correlations.

Fig. 8 shows the generally accepted ground state of $La_{0.5}Sr_{1.5}MnO_4$ displaying charge, spin and orbital ordering in the basal MnO_2 planes. The high-temperature $I4/mmm$ unit cell is shown by the solid line ($a = b = 3.864$ Å and $c = 12.40$ Å). The occurrence of orbital order reflections with a wavevector of $(\frac{1}{4}, \frac{1}{4}, 0)$ shows that the orbital ordering causes the unit cell to quadruple in the ab plane. The new orbital ordered unit cell is shown by the dashed lines.

Variable-temperature scans of the magnetic and orbital reflections were undertaken at beamline 5U1 at Daresbury Laboratory. Fig. 9 (upper) shows the integrated intensity of features at 643 and 653 eV in the $(\frac{1}{4}, \frac{1}{4}, 0)$ orbital reflection as a function of temperature. As discussed in our earlier paper (Wilkins *et al.*, 2003) and by Wilkins *et al.* (2004), scattering at the Mn L_{III} edge ($\sim$643 eV) is primarily associated with cooperative Jahn–Teller distortions. Those at the Mn L_{II} ($\sim$653 eV) edge are primarily associated with direct Goodenough orbital ordering. As can be seen, the features associated with the Jahn–Teller distortions are greatest at all temperatures below the orbital ordering temperature (T_{OO}). Close to T_{OO} the features are of more nearly equal intensity. This means that at T_{OO}, orbital order correlations caused by antiferromagnetic spin correlations are almost as important as the effects of the cooperative Jahn–Teller distortions in determining the long-range orbital ordering. However, upon further cooling the features at the Mn L_{III} edge grow with respect to those features at the L_{II} edge. Therefore, although both Jahn–Teller distortions and antiferromagnetic orbital interactions increase as the temperature is lowered, those owing to Jahn–Teller distortions increase at a greater rate. Of course, the extent of the Jahn–Teller distortions would be expected to increase as the temperature is lowered. However, although X-ray measurements show the Jahn–Teller distortions to have maximized by $\sim$150 K, the effect of the Jahn–Teller distortions on the long-range orbital correlations continues to grow, both absolutely and with respect to the antiferromagnetic orbital correlations. At T_N ($\sim$110 K) an

abrupt and unexpected increase in the intensity of the orbital order reflection is noted. There occurs a stepwise increase at both Mn L edges. Fig. 9 (lower) shows the branching ratio, *i.e.* the ratio of the intensity of the L_{III} features over that of the L_{II} features. This ratio is always above 1.0 (Jahn–Teller features dominant) but maximizes at almost 2.5 at T_N, before decreasing somewhat.

The dramatic increase in the intensity of the orbital ordering reflection at T_N is very unexpected. This suggests that the long-range orbital ordering interactions are only maximized below T_N. The Néel temperature is also the temperature at which the Jahn–Teller contribution to the orbital correlations is at its greatest. The region between T_{OO} and T_N is one in which the orbital order correlations gradually increase with decreasing temperature. It is only at T_N, at which the antiferromagnetic spin correlations become established throughout the whole crystal, that the long-range orbital correlations are maximized. As the temperature is lowered below T_N the orbital correlations are approximately constant in intensity, even as the antiferromagnetic spin correlations are gradually increasing. Is such behaviour typical, or special just to $La_{0.5}Sr_{1.5}MnO_4$? Because this is one of the first studies to directly measure orbital and magnetic correlations in any material, it is difficult to be certain. There are, however, intriguing results obtained by resonant X-ray studies at the K
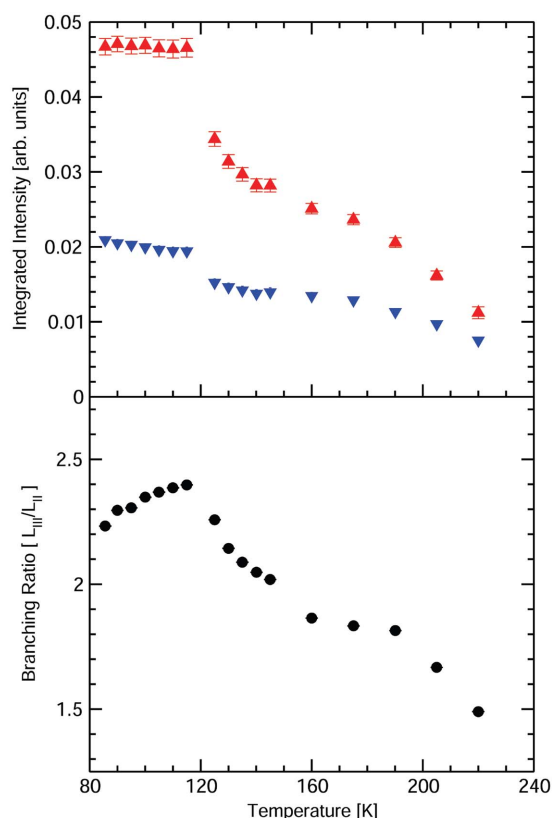

Figure 9
Top: integrated intensity of the $(\frac{1}{4}, \frac{1}{4}, 0)$ reflection in $La_{0.5}Sr_{1.5}MnO_4$ showing the intensity of the peak at 643 eV (triangles) and 654 eV (inverted triangles). There is a distinct step at T_N, and also the branching ratio (bottom) reaches a maximum at T_N. Errors in the fits are within the symbol size.

absorption edge that such effects may be a general feature of strongly correlated $3d$ transition metal compounds. Such results have not directly probed the $3d$ band. Rather, as discussed above, K-edge studies probe the $4p$ band and hence we need to infer, in a rather indirect way, that changes in the $4p$ band may reflect changes to the $3d$ band caused by orbital interactions. In LaMnO$_3$, RXS studies at the Mn K edge showed scattering at a wavevector of (1,0,0) around allowed Bragg positions. Intensity measurements showed that this scattering, indirectly associated with orbital ordering *via* Jahn–Teller distortions of the crystal structure, increased dramatically at T_{OO} (~ 780 K) and thereafter remained almost constant until just above T_N (~ 140 K). Just above T_N the intensity increased by $\sim 50\%$ and remained constant between T_N and the base temperature (Murakami *et al.*, 1998). In KCuF$_3$ a doubling in the intensity of the (331) orbital order reflection was observed just above T_N (~ 38 K), and again remaining constant below T_N (Paolasini *et al.*, 2002). This is similar to La$_{0.5}$Sr$_{1.5}$MnO$_4$ where we observe a doubling of the $(\frac{1}{4}, \frac{1}{4}, 0)$ orbital reflection just above T_N. Ishihara & Maekawa (2000) suggested that such anomalous changes in the intensity of the orbital order reflection may signal a change in the type of orbital order near the magnetic transition. However, the resonant soft X-ray energy scans are very sensitive to the type of orbital order, as demonstrated by the theoretical calculations of Castleton & Altarelli (2000). Energy scans taken above and below T_N show no dramatic changes suggesting any such change. Rather, there is a continuous change in intensity and spectral weight.

Finally we consider the first-order transition at T_{OO} (= T_{CO} $\simeq 240$ K). Fig. 9 displays the intensity of the $(\frac{1}{4}, \frac{1}{4}, 0)$ orbital reflection at the Mn L_{III} (primarily caused by Jahn–Teller distortions) and Mn L_{II} (primarily caused by direct Goodenough orbital ordering) edges in the vicinity of T_{OO}. Because of the first-order nature of this transition we did not observe any critical scattering caused by orbitally ordered critical fluctuations above T_{OO}. However, below T_{OO} the order parameters of the two separable causes of orbital ordering are very different. This suggests that at T_{OO} the spin correlations have the largest relative contribution at any temperature. This suggests that short-range Goodenough antiferromagnetic spin interactions may indeed be the root cause of the transition into the charge and orbitally ordered state. Once this is formed, Jahn–Teller distortions occur and further strengthen the long-range orbital correlations. Long-range antiferromagnetism is not realised until much lower temperatures and is accompanied by another increase in the intensity of the orbital ordering.

5. Conclusions

In conclusion, soft X-ray resonant diffraction has been used to directly observe changes in the intensity of allowed Bragg reflections. Such strong resonances have been used to directly observe the antiferromagnetic ordering of $3d$ spins and even the formation and development of orbital order in doped manganites. Our studies have demonstrated the wealth of information that is only observable using soft X-ray diffraction. Even in materials where the Ewald sphere is so small, soft X-ray diffraction has the remarkable ability to probe simultaneously the different facets of electron correlations.

References

Abbamonte, P., Venema, L., Rusydi, A., Sawatzky, G. A., Logvenov, G. & Bozovic, I. (2002). *Science*, **297**, 581.

Als-Nielsen, J. & McMorrow, D. (2001). *Elements of Modern X-ray Physics.* New York: Wiley.

Benedetti, P., van den Brink, J., Pavarini, E., Vigliante, A. & Wochner, P. (2001). *Phys. Rev. B*, **63**, 060408.

Benfatto, M., Joly, Y. & Natoli, C. R. (1999). *Phys. Rev. Lett.* **83**, 636–639.

Bergevin, F. de & Brunel, M. (1981). *Acta Cryst.* A**37**, 314.

Blume, M. (1985). *J. Appl. Phys.* **57**, 3615–3618.

Blume, M. & Gibbs, D. (1988). *Phys. Rev. B*, **37**, 1779–1789.

Blume, M. & Gibbs, D. (1989). *Phys. Rev. B*, **40**, 5218.

Castleton, C. W. M. & Altarelli, M. (2000). *Phys. Rev. B*, **62**, 1033–1038.

Daoud-Aladine, A., Rodriguez-Carvajal, J., Pinsard-Gaudart, L., Fernandez-Diaz, M. T. & Revcolevschi, A. (2002). *Phys. Rev. Lett.* **89**, 097205.

Dhesi, S. S., Mirone, A., De Nadai, C., Ohresser, P., Bencok, P., Brookes, N. B., Reutler, P., Revcolevschi, A., Tagliaferri, A., Toulemonde, O. & van der Laan, G. (2004). *Phys. Rev. Lett.* **92**, 056403.

Elfimov, I. S., Anisimov, V. I. & Sawatzky, G. A. (1999). *Phys. Rev. Lett.* **82**, 4264–4267.

Fourme, R., Shepard, W., Kahn, R., l'Hermite, G. & Li de La Sierra, I. (1995). *J. Synchrotron Rad.* **2**, 36.

Gibbs, D., Harshman, D. R., Isaacs, E. D., McWhan, D. B., Mills, D. & Vettier, C. (1988). *Phys. Rev. Lett.* **61**, 1241–1244.

Goodenough, J. B. (1955). *Phys. Rev.* **100**, 564.

Hannon, J. P., Trammel, G. T., Blume, M. & Gibbs, D. (1988). *Phys. Rev. Lett.* **61**, 1245.

Hatton, P. D., Wilkins, S. B., Spencer, P. D., von Zimmermann, M. & d'Almeida, T. (2003). *J. Phys. D*, **36**, A157–A161.

Hill, J. P. & McMorrow, D. F. (1996). *Acta Cryst.* A**52**, 236.

Isaacs, E. D., McWhan, D. B., Peters, C., Ice, G. E., Siddons, D. P., Hastings, J. B., Vettier, C. & Vogt O. (1989). *Phys. Rev. Lett.* **62**, 1671–1674.

Ishihara, S. & Maekawa, S. (2000). *Phys. Rev. B*, **62**, R9252–R9255.

Ling, C. D., Millburn, J. E., Mitchell, J. F., Argyriou, D. N., Linton, J. & Bordallo, H. N. (2000). *Phys. Rev. B*, **62**, 15096–15111.

Mizokawa, T. & Fujimori, A. (1997). *Phys. Rev. B*, **56**, R493–R496.

Moritomo, Y., Asamitsu, A., Kuwahara, H. & Tokura, Y. (1996). *Nature (London)*, **380**, 141.

Murakami, Y., Hill, J. P., Gibbs, D., Blume, M., Koyama, I., Tanaka, M., Kawata, H., Arima, T., Tokura, Y., Hirota, K. & Endoh, Y. (1998). *Phys. Rev. Lett.* **81**, 582.

Murakami, Y., Kawada, H., Kawata, H., Tanaka, M., Arima, T., Moritomo, Y. & Tokura, Y. (1998). *Phys. Rev. Lett.* **80**, 1932–1935.

Paixao, J. A., Detlefs, C., Longfield, M. J., Caciuffo, R., Santini, P., Bernhoeft, N., Rebizant, J. & Lander, G. H. (2002). *Phys. Rev. Lett.* **89**, 187202.

Paolasini, L., Caciuffo, R., Sollier, A., Ghigna, P. & Altarelli, M. (2002). *Phys. Rev. Lett.* **88**, 106403.

Roper, M. D., van der Laan, G., Dürr, A., Dudzik, E., Collins, S. P., Miller, M. C. & Thompson, S. P. (2001). *Nucl. Instrum. Methods Phys. Res. A*, **467/468**, 1101–1104.

Solovyev, I. V. & Terakura, K. (1999). *Phys. Rev. Lett.* **83**, 2825–2828.

Sternlieb, B. J., Hill, J. P., Wildgruber, U. C., Luke, G. M., Nachumi, B., Moritomo, Y. & Tokura, Y. (1996). *Phys. Rev. Lett.* **76**, 2169–2172.

Thomas, K. J., Hill, J. P., Grenier, S., Kim, Y.-J., Abbamonte, P., Venema, L., Rusydi, A., Tomioka, Y., Tokura, Y., McMorrow, D. F., Sawatzky, G. & van Veenendaal, M. (2004). *Phys. Rev. Lett.* **92**, 237204.

Tokura, Y. & Nagaosa, N. (2000). *Science*, **288**, 462.

Wakabayashi, Y., Murakami, Y., Koyama, I., Kimura, T., Tokura, Y., Moritomo, Y., Hirota, K. & Endoh, Y. (2000). *J. Phys. Soc. Jpn*, **69**, 2731.

Weiss, M. S., Sicker, T., Djinovic Carugo, K. & Hilgenfeld, R. (2001). *Acta Cryst.* D**57**, 689–695.

Weschke, E., Ott, H., Schierle, E., Schussler-Langeheine, C., Vyalikh, D. V., Kaindl, G., Leiner, V., Ay, M., Schmitte, T., Zabel, H. & Jensen, P. J. (2004). *Phys. Rev. Lett.* **93**, 157204.

Wilkins, S. B., Hatton, P. D., Roper, M. D., Prabhakaran, D. & Boothroyd, A. T. (2003). *Phys. Rev. Lett.* **90**, 187201.

Wilkins, S. B., Spencer, P. D., Beale, T. A. W., Hatton, P. D., v. Zimmermann, M., Brown, S. D., Prabhakaran, D. & Boothroyd, A. T. (2003). *Phys. Rev. B*, **67**, 205110.

Wilkins, S. B., Spencer, P. D., Hatton, P. D., Collins, S. P., Roper, M. D., Prabhakaran, D. & Boothroyd, A. T. (2003). *Phys. Rev. Lett.* **91**, 167205.

Wilkins, S. B., Stojic, N., Beale, T. A. W., Binggeli, N., Castleton, C. W. M., Bencok, P., Prabhakaran, D., Boothroyd, A. T., Hatton, P. & Altarelli, M. (2004). *Condensed Matter preprint server, Strongly Correlated Electrons* 0410713.